Research Square

Preprints are preliminary reports that have not undergone peer review.
They should not be considered conclusive, used to inform clinical practice,
or referenced by the media as validated information.

Mechanical relaxation: soft modes of the joint cell–atom Hessian connect crystal structure prediction with the unstable lattices of CALPHAD

Pavlo Prysiazhniuk

pavlo.prysiazhniuk@nung.edu.ua

Ivano-Frankivsk National Technical University of Oil and Gas

Thaer Abdulwahhab Shihab

Al-Bayan University

Alina Zakrjevsky

Queen Mary University of London

Gregory A. Chass

McMaster UniversityDepartment of Chemistry and Chemical Biology

Article

Keywords: crystal structure prediction, soft modes, joint cell–atom Hessian, saddle points, lattice stability, CALPHAD

Posted Date: November 24th, 2026

DOI: https://doi.org/10.21203/rs.3.rs-11571854/v1

License: This work is licensed under a Creative Commons Attribution 4.0 International License.
Read Full License

Additional Declarations: No competing interests reported.

Mechanical relaxation: soft modes of the joint cell–atom Hessian connect crystal structure prediction with the unstable lattices of CALPHAD

Pavlo Prysiazhniuk[1*], Thaer Abdulwahhab Shihab[2], Alina Zakrjevsky[3], Gregory A. Chass[4,5,6]

[1*]Department of Computerized Mechanical Engineering, Ivano-Frankivsk National Technical University of Oil and Gas, 15 Karpatska St., Ivano-Frankivsk, 76019, Ukraine.
[2]Technical Engineering College, Al-Bayan University, International Airport St., Near Abbas Ibn Firnas Square, 6111, Baghdad, 10070, Iraq.
[3]School of Physical and Chemical Sciences, Queen Mary University of London, Mile End Road, London, E1 4NS, United Kingdom.
[4]Department of Chemistry and Chemical Biology, McMaster University, Hamilton, Ontario, Canada.
[5]Mesoscale Engineering Halcyon Srl (MEH), Rome, Italy.
[6]Mesoscale Energy Halcyon Canada Inc (MEH-Canada), Alberta Carbon Conversion Technology Centre (ACCTC), Calgary, Alberta, Canada.

*Corresponding author(s). E-mail(s): pavlo.prysiazhniuk@nung.edu.ua;

Abstract

Ordinary geometry relaxation cannot leave a high-symmetry saddle point, because forces and stresses vanish there by symmetry. We replace it with *mechanical relaxation*: deterministic pushes along the softest eigenmode of the joint cell–atom Hessian, repeated until no unstable mode remains in the cell. Every push splits into a strain part, which is the elastic-tensor mode of tensor-guided lattice exploration, and a shuffle part. From 1221 random symmetric structures of eleven elements, ordinary relaxation ends on a saddle in 74 % of cases, and mechanical relaxation increases the number of runs that reach the reference structure from 50 to 221. The trajectories funnel through a small set of high-symmetry saddle hubs. For As, Sb and Bi the hub is the simple-cubic lattice, and a single shuffle reproduces the Peierls route to A7. The hubs include the mechanically unstable lattices of CALPHAD, saddle points whose order grows in

proportion to the number of atoms. Their lattice stabilities, where obtained by phase-diagram extrapolation, fall into two regimes and follow the static energy along the softest-mode path, not the fraction of the Brillouin zone in which the lattice is unstable.

Keywords: crystal structure prediction, soft modes, joint cell–atom Hessian, saddle points, lattice stability, CALPHAD

Introduction

Crystal structure prediction (CSP) is organised around minima of the potential energy surface. Random structure searching [1], evolutionary algorithms [2, 3] and their many descendants generate candidates, relax them to the nearest minimum and rank the minima. Saddle points are by-products, and are discarded. The workhorse step is ordinary geometry relaxation: a gradient method in atomic coordinates and cell parameters. Started from a symmetric structure, it preserves the symmetry, because the forces and stresses inherit it. If the symmetric structure sits on a saddle, the relaxation stops there. This has long been known [1, 4, 5]. It is usually treated as a nuisance, removed by a random "shake" or by following an imaginary phonon [1, 6]. It has also been exploited on purpose: saddle-point ab initio random structure searching (AIRSS) imposes symmetry to land on saddles as candidates for high-temperature phases [7].

Following imaginary phonons from a high-symmetry parent is an established route to lower-symmetry structures [6, 8–10]. Togo and Tanaka built trees of transition pathways from the simple-cubic structure of seven metals [8]. Naruse, Seko and Tanaka followed imaginary modes with machine-learning potentials for Cu, Ag and Au [9] and, later, Si [10]. Group-theoretical enumerations of transition mechanisms [11, 12] and soft-mode mutations in evolutionary searches [2, 3] rest on the same idea. Leaving a symmetric saddle is therefore not new. What has not been done, to our knowledge, is to follow the *joint* cell–atom Hessian from many random symmetric starts, to count how often ordinary relaxation fails, and to map the saddles through which the trajectories pass.

The thermodynamics of alloys needs exactly these saddle points. CALPHAD (calculation of phase diagrams) databases assign Gibbs energies to the elements in crystal structures that are mechanically unstable, such as bcc Ru, fcc W and hcp Mo, because solid solutions of other elements are stable in those structures. The SGTE (Scientific Group Thermodata Europe) values of these lattice stabilities [13] disagree with first-principles static energies, sometimes by a factor of two or three [14–16]. The disagreement has been traced to the absence of a well-defined harmonic free energy for an unstable lattice [16, 17]. Remedies include anharmonic or self-consistent lattice dynamics [18–22], inflection-point constructions [17, 23, 24] and complex-structure calculations [25, 26]. In energy-landscape language, these lattices are saddle points of the very surface that CSP explores [27, 28].

We start from tensor-guided lattice exploration (TGLE), a CSP scheme in which a structure is deformed along the softest eigenvector of its 6×6 elastic stiffness tensor,

with the atoms relaxed at every step [29]. Here the step is generalised to the softest eigenmode of the joint cell–atom Hessian and applied repeatedly until the structure is mechanically stable within its cell. We call this *mechanical relaxation*. We test it on a blind set of starting space groups, identical for all elements, against ordinary relaxation and three alternative schemes at equal cost; map the saddle hubs through which the trajectories funnel, which reproduces the Peierls route from simple cubic to A7 for As, Sb and Bi; show that the unstable CALPHAD lattices are saddle points of extensive order; and ask what the extent of their instability controls in the thermodynamics of the lattice.

Results

Ordinary relaxation stops at saddles; mechanical relaxation leaves them

All descents use the foundation machine-learning interatomic potential GRACE-2L-OMAT [30, 31]; ordinary relaxation is the Broyden–Fletcher–Goldfarb–Shanno (BFGS) algorithm, and density functional theory (DFT) checks the key structures and Hessians (Methods). Figure 1 shows the mechanism on a four-atom start of Ge in $P6_3/mmc$. BFGS descends from +206 kJ/mol to a saddle at +40.2 kJ/mol that has the volume and, on average, the fourfold coordination of diamond. It is not diamond, because its bonds are stretched (2.56 versus 2.48 Å) and their topology is wrong, and it still has four unstable subspaces. The first push is a pure shuffle ($c_w = 0$). It breaks the screw axis, $P6_3/mmc \rightarrow P\bar{3}m1$, and leads to a second saddle at +20.8 kJ/mol. The second push is a coupled cell shear ($c_w = 0.40$): the monoclinic angle opens from 90° to 106.8° and the structure becomes diamond. The volume stays within 3 % throughout. The energy is gained from bond angles and topology, not from density.

Figure 2 and Table 1 give the blind-set statistics. Of 1221 starts, 903 (74 %) end on a saddle after BFGS, that is, with at least one unstable mode of the joint Hessian in the cell. Ordinary relaxation reaches the SGTE reference structure 50 times (4.1 %) and mechanical relaxation 221 times (18.1 %). If starts in the space group of the reference are excluded, the counts are 42 and 206 of 1176, so the gain does not come from a hint in the starting symmetry. Only 17 runs (1.4 %) remain unresolved: the push along the softest mode did not lower the energy at any amplitude, or the descent tripped the collapse guard, so an unstable mode remains; 64 runs end in triclinic minima, which we count as minima. The gain is largest where the reference is a distorted high-symmetry lattice: Ti (5→47 hits), Bi (1→36), Sb (1→34) and As (0→16). It is smallest for Sn and Ga (0→2 and 0→0). Their references (A5 and α-Ga) are surrounded by many nearly degenerate minima, and mechanical relaxation ends in one of them.

Most runs end neither in the reference nor unresolved, but in another local minimum (Fig. 2). Some are known polymorphs: lonsdaleite for Si and Ge, α-Sn, fcc and ω for Ti, and the simple-hexagonal high-pressure phase of Si, which is a local minimum of the potential in small cells. Others are high-energy minima of small cells. Five end points lie below the reference on the potential: a $P2_1/m$ structure of U (−0.5 kJ/mol), a $P\bar{3}m1$ structure of As (−0.4), lonsdaleite Si (−0.1), and $P4/nmm$ and $Pnma$ structures of U (−0.1 and −0.07). DFT places lonsdaleite Si, the $P\bar{3}m1$

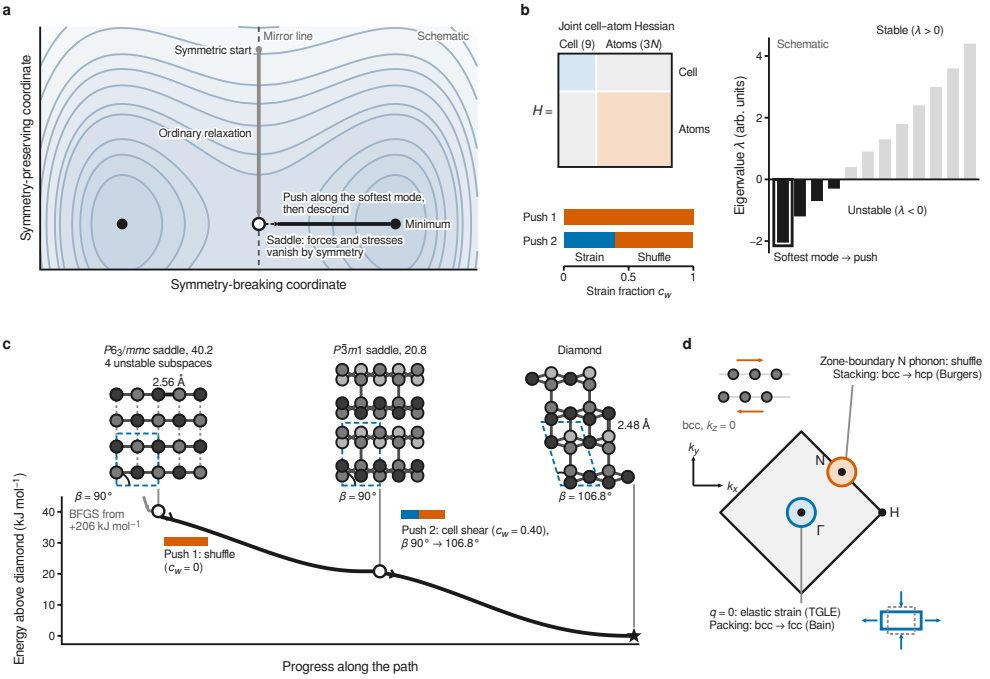

Fig. 1 Mechanical relaxation. (a) Ordinary relaxation from a symmetric start halts at a saddle where forces and stresses vanish by symmetry; a push along the softest mode followed by a descent reaches a minimum (schematic surface). (b) Block structure of the joint cell–atom Hessian, a schematic spectrum at a saddle, and the strain fraction c_w (squared norm of the cell components of the mode) of the two pushes of panel (c). (c) Ge: a four-atom $P6_3/mmc$ start descends through the saddles $P6_3/mmc$ (40.2 kJ/mol) and $P\bar{3}m1$ (20.8 kJ/mol) to diamond; the first push is a pure shuffle, the second a cell shear. Insets: the three stationary structures on a common scale, viewed along the normal to the plane of the lattice vectors **a** and **c** (dashed: unit cell; β: cell angle). (d) In reciprocal space the elastic-tensor modes ($\mathbf{q} = 0$) change the packing (Bain, bcc→fcc), whereas zone-boundary phonons such as N change the stacking (Burgers, bcc→hcp); insets: the corresponding real-space distortions.

structure of As and the $P4/nmm$ structure of U above the reference (Supplementary Table S14); these mark the limits of the potential rather than new ground states. The $P2_1/m$ structure of U keeps its space group at any symmetry tolerance up to 0.5 Å and lies within 0.1 kJ/mol of α-U in DFT, degenerate within the accuracy of the present scalar-relativistic, non-magnetic PBE setting. Within the explored cells, mechanical relaxation is therefore a deterministic mapping of the minima around the saddle network, not only a search for the ground state.

Comparison with alternative schemes at accounted cost

We compare mechanical relaxation with three alternatives on the same blind starts, all beginning from the BFGS end point and all charged with every force evaluation, including those spent on Hessians (Methods): following the unstable modes of the fixed-cell atomic Hessian, which is the scheme of Togo and Tanaka [8]; following the unstable strain modes only, which is the elastic step of TGLE; and random pushes of

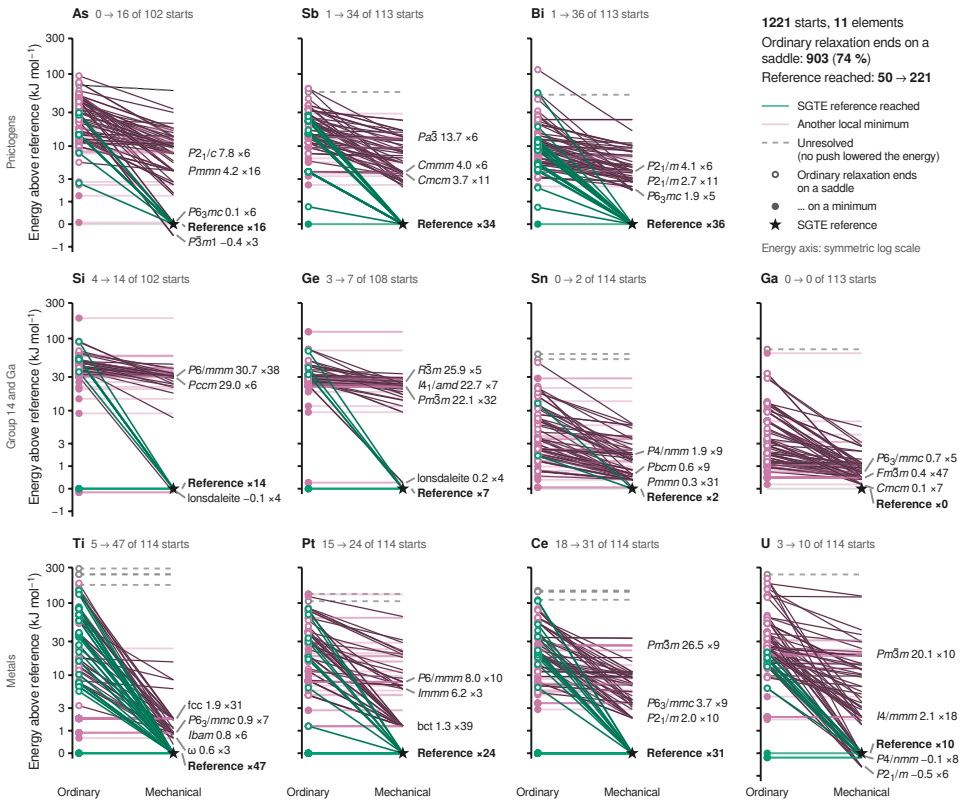

Fig. 2 Outcomes of all descents from the blind set of starting space groups (GRACE-2L-OMAT). Each line is one start and joins the end of ordinary relaxation (left; open circle: saddle, filled circle: minimum) to the end of mechanical relaxation (right). Green: SGTE reference (star) reached; purple: another local minimum with no unstable mode in the cell; grey dashed: unresolved. Headers: reference hits after ordinary → after mechanical relaxation, and the number of starts. Labels: the most frequent end points, with their energies in kJ/mol above the reference and the number of runs. The energy axis is symmetric logarithmic and common to all panels.

the same amplitudes. Figure 3 and Supplementary Table S13 give the result for 931 blind starts of all eleven elements with $N = 4$, 8 and 12. Ordinary relaxation alone reaches the reference in 47 starts; the 884 remaining starts are the task, and we count hits among them. Random pushes solve most of them, 183 and 184 per realisation and 214 for either of two (the realisations disagree on 61 starts), but at a median cost of 18 600 evaluations per start against 2 000 for the joint Hessian, and 90 000 evaluations per hit against 36 000. At equal budget the order reverses (Fig. 3d): with at most 10^4 evaluations per start the joint Hessian solves 92 starts, the fixed-cell atomic modes with the same candidate scan 82, the strain modes 27 and a random push 46–49; random pushes overtake between 10^4 and 3×10^4 evaluations per start. Fixed-cell mode following with the same candidate scan and the same three descents per push comes close to the joint Hessian: 110 against 126 new hits (McNemar's test on the discordant starts, 23 against 7, $p = 0.005$) at the same cost per hit (0.29 against 0.28

Table 1 Blind-set statistics (GRACE-2L-OMAT). "Saddle": BFGS end point with at least one unstable mode of the joint Hessian. Hits: runs that end in the SGTE reference structure. "Other minima" includes triclinic ones (in parentheses). "Unresolved": an unstable mode remains because no push lowered the energy (see text).

Element	Starts	Saddle	Hits (BFGS)	Hits (mechanical)	Other minima	Unresolved
Ti	114	82	5	47	63 (0)	4
Bi	113	107	1	36	76 (10)	1
Sb	113	101	1	34	78 (11)	1
Ce	114	70	18	31	79 (4)	4
Pt	114	67	15	24	88 (6)	2
As	102	87	0	16	85 (12)	1
Si	102	65	4	14	88 (2)	0
U	114	82	3	10	103 (6)	1
Ge	108	68	3	7	101 (6)	0
Sn	114	90	0	2	110 (4)	2
Ga	113	84	0	0	112 (3)	1
Total	1221	903	50	221	983 (64)	17

hits per 10^4 evaluations). The gain is concentrated in the smallest cells and in As, Sb and Bi, where the cell shear that completes the Peierls route couples to the shuffle (50 against 39 new hits at $N = 4$, 49 against 45 at $N = 8$, 27 against 26 at $N = 12$); for Ti, Ce and Pt the two schemes are equal. Following the strain modes alone solves 46 starts, half of the joint Hessian, but costs almost nothing (median 19 evaluations, 18 000 per hit), and it is the best scheme for Pt, where the route to fcc is a pure Bain strain (28 against 17 hits). Mechanical relaxation is therefore not the scheme with the most hits. It is the deterministic one that labels every step by its strain fraction, keeps strain and shuffle in one eigenproblem, is the most efficient scheme at budgets up to 10^4 evaluations per start, and costs 2.5 times less per hit than random pushes.

Paths: strain changes the packing, shuffles change the stacking

Supplementary Figure S2 shows representative paths, and Supplementary Fig. S3 the first descent from 63 mechanically unstable fcc, bcc and hcp element lattices, which follows the softest mode of the smallest cell. A pure strain seed ($c_w = 1$), exactly the step of TGLE [29], reaches the reference for every Bain-type transition, fcc↔bcc, including the cases where the Bain path bifurcates (Nb, V, Ta). From bcc, however, it always ends in fcc, never in hcp (15 of 15): it finds the close-packed density but not the stacking; fcc lies 0.1–13 kJ/mol above hcp. Hcp is reached only by the next attempt, a pure shuffle ($c_w = 0$, the zone-boundary N phonon) in a two-atom cell, with the cell strain developing during the descent; this happened in all 19 late hits. For La and Nd the double-hcp reference is found in a four-atom cell by the *second* softest mode, while the softest one leads to hcp (0.9 kJ/mol above). For these close-packed metals the rule "strain changes the packing, shuffles change the stacking" is the real-space form of a reciprocal-space fact: packing changes are long-wavelength strains ($\mathbf{q} = 0$), and stacking changes are zone-boundary phonons. We do not claim it as a general law. Along the full mechanical-relaxation paths the order is often reversed:

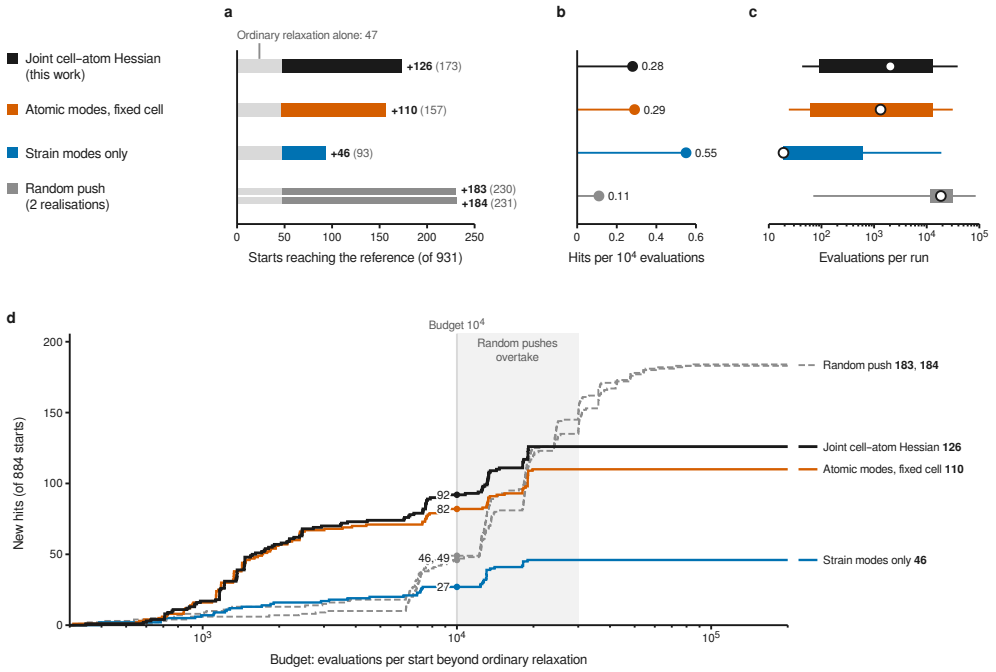

Fig. 3 Alternative schemes at accounted cost on the 931 common blind starts (GRACE-2L-OMAT), all starting from the BFGS end point. Atomic modes and strain modes use the same candidate scan and three descents per push as the joint Hessian; random pushes have two realisations. (a) Starts reaching the reference: by BFGS alone (light segment, 47) and in addition by each scheme (new hits; total in parentheses). The new hits of the three Hessian-based schemes all come from the 685 starts where BFGS ends on a saddle. (b) Hits per 10^4 evaluations beyond BFGS. (c) Evaluations per run, including Hessians: median (open circle), interquartile range (bar) and full range (line). (d) Equal budget: new hits among the 884 starts not solved by BFGS within a given number of evaluations per start; the values at 10^4 evaluations are marked, and the shaded band shows where random pushes overtake.

shuffles rebuild the bonds first and a cell shear completes the transition, as for Ti, Pt, U and the Ge example of Fig. 1 (Supplementary Fig. S2). For the pnictogens a single shuffle suffices, and for many Si and Ge paths both steps are shuffles between simple-hexagonal saddles.

A network of saddle hubs and the Peierls route

Independent starts do not wander. They funnel through a small number of high-symmetry saddles (Fig. 4):

- As, Sb and Bi: the simple-cubic lattice ($Pm\bar{3}m$; 14.6, 4.0 and 5.2 kJ/mol above A7, crossed by 12, 24 and 13 trajectories of the blind set);
- Ti: bct (6.7 kJ/mol, 10 trajectories) and bcc (7.7 kJ/mol, 7 trajectories), with fcc as an intermediate minimum (1.9 kJ/mol, 31 trajectories);
- Si and Ge: simple hexagonal ($P6/mmm$; 30.7 and 23.0 kJ/mol, 39 and 10 trajectories), with simple cubic for Si (32.5 kJ/mol, 13 trajectories, 12 of them through the

saddle). The node counts include a two-atom AA-stacked honeycomb at the energy of the simple-hexagonal node (Methods).

The pnictogen case is a test of the method against known physics. The Peierls distortion, which halves the coordination from six to three, has long been understood as the electronic origin of the A7 structure [32–34], and Needs, Martin and Nielsen showed that simple-cubic As is unstable towards A7 phonon displacements at every pressure [32]. Mechanical relaxation was given nothing beyond the energy surface and reproduced this route automatically: 49 trajectories of the blind set pass through the simple-cubic hub of a pnictogen, starting from unrelated space groups such as $Pnma$ and $I4/mmm$. In 42 of them the next push, a pure shuffle ($c_w < 0.001$), leads straight to A7; the remaining seven (six Sb, one Bi) end in $Cmmm$, $Pmma$ or $I2_13$ minima 4–4.5 kJ/mol above A7. The saddle hubs overlap with the lattices used as CALPHAD end members: simple cubic for the pnictogens, fcc, bcc, hcp and bct for the metals. Of the 56 saddle hubs crossed by at least three trajectories in the six elements of Fig. 4, 34 are of these types; most of the others are orthorhombic ($Cmcm$, $Cmmm$, $Pmma$, $Imma$) or simple hexagonal. The hub energies are not artefacts of the potential (Supplementary Table S14): DFT reproduces the simple-cubic hubs of Sb and Bi and the simple-hexagonal hubs of Si and Ge to within 1 kJ/mol, whereas GRACE overestimates simple-cubic As by 4 kJ/mol and underestimates the bct saddle of Ti by 2.6 kJ/mol.

Unstable lattices are saddle points of extensive order

How unstable is a CALPHAD lattice? Figure 5 counts the negative eigenvalues of the joint Hessian of ideal lattices in supercells of increasing size. For every mechanically unstable phase the count grows roughly in proportion to N. For bcc Ti it is 2, 8, 22 and 44 at $N = 1$, 8, 27 and 64. For the stable phases (hcp Ti up to 96 atoms, fcc Ti and bcc W up to 64 atoms) it is exactly zero. A first-order transition state, by contrast, has order one at any N. The unstable lattices of CALPHAD thus form a distinct class of critical points: saddles of extensive order. They lie on no minimum-energy path between minima, so methods designed for first-order saddles (nudged elastic band, dimer) are not designed to find them. It also explains why a lattice stability defined along a path depends on the path: an extensive number of descent directions leave the saddle. Extensive saddle orders are familiar in the landscape theory of liquids [35–38]. For crystals, van de Walle et al. noted that the number of unstable modes is zero, small, or scales with system size [17]. We are not aware of a measurement of this scaling for ideal crystal lattices, nor of its use to classify structures.

The count is reproduced by DFT (Table 2). In $3 \times 3 \times 3$ supercells at fixed cell, bcc Cu, bcc Pd, fcc W, bcc Ti, bcc Rh and bcc Al have 12, 12, 16, 20, 20 and 12 imaginary phonon modes in DFT; the atomic block of the GRACE Hessian at the same cell gives the same numbers. This validates the mode count on a finite grid. A direct test of f_{BZ} itself, from DFT force constants of the same cell interpolated exactly as for the potential (Methods; Table 2, right), shows that DFT and GRACE agree on the extent of the instability for all six lattices, from the weakly unstable bcc Cu and Pd to the strongly unstable bcc Ti, Rh and Al; the largest difference is fcc W

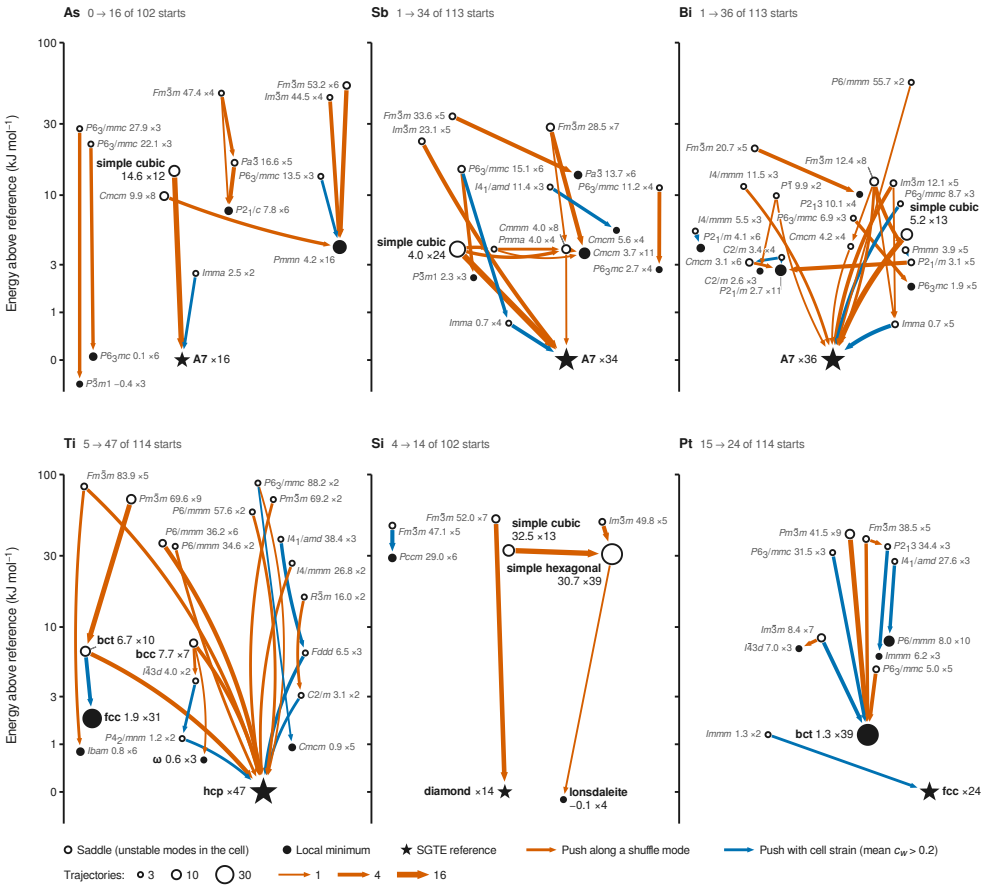

Fig. 4 Saddle hubs visited by mechanical relaxation (blind set, six elements; the other five elements in Supplementary Fig. S1). A node is a space group at a given energy (0.5 kJ/mol bins); shown are the nodes crossed by at least three trajectories and the nodes crossed by two trajectories on paths that reach the reference. Vertical position: mean energy above the reference, on a symmetric logarithmic scale common to all panels; labels give this energy in kJ/mol and the number of trajectories. Open circles: saddles; filled circles: minima; star: SGTE reference. Marker area and arrow width scale with the number of trajectories. Vermilion arrows: pushes along shuffle modes; blue arrows: pushes with cell strain (mean $c_w > 0.2$). Headers: reference hits after ordinary → after mechanical relaxation, and the number of starts.

(0.22 versus 0.17). The deepest eigenvalues agree within 15 % except for bcc Ti, where GRACE is shallower (-2.42 versus $-3.78\,\mathrm{eV\,Å^{-2}}$). With $4 \times 4 \times 4$ force constants, whose grid contains the zone-boundary point X that the $3 \times 3 \times 3$ grid lacks, DFT and GRACE agree for bcc Cu ($f_{\mathrm{BZ}} = 0.032$ against 0.030) but part for fcc W ($f_{\mathrm{BZ}} = 0.45$ against 0.30, $\lambda_{\min} = -5.8$ against $-3.1\,\mathrm{eV\,Å^{-2}}$; Supplementary Table S8). The X-point instability of fcc W is where the potential errs most, by a factor of two in depth, and the $3 \times 3 \times 3$ grid, which does not contain X, hid this. For bcc Ti the two $4 \times 4 \times 4$ grids agree on the extent of the instability ($f_{\mathrm{BZ}} = 0.60$ against 0.59) and differ in its depth ($\lambda_{\min} = -4.9$ against $-2.6\,\mathrm{eV\,Å^{-2}}$), as on the $3 \times 3 \times 3$ grid.

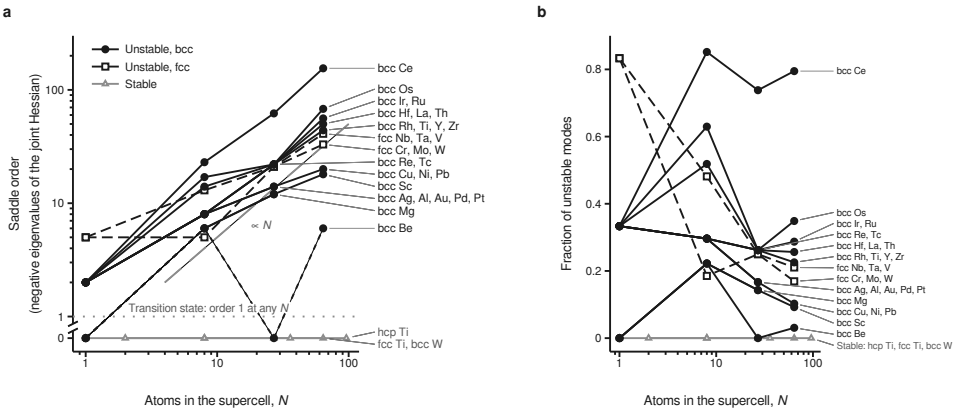

Fig. 5 Saddle order of ideal lattices versus supercell size (GRACE-2L-OMAT; $n \times n \times n$ supercells of N atoms). (a) Number of negative eigenvalues n_- of the joint cell–atom Hessian; it grows $\propto N$ for unstable phases and is exactly zero for stable ones (bottom row, below the axis break; dotted segments lead to zero). Phases with identical sequences share a line. Dotted horizontal line: order 1, that of a transition state. (b) Fraction of unstable modes, $n_-/(3N+3)$ (three translations removed from the $3N+6$ coordinates), which tends to f_{modes}.

Table 2 DFT versus GRACE-2L-OMAT for ideal lattices in $3 \times 3 \times 3$ supercells at fixed cell. Left: imaginary phonon modes (of 78 non-translational modes) and DFT imaginary frequencies (cm^{-1}); GRACE values are for the atomic block of its Hessian at the DFT cell. Right: unstable zone fraction f_{BZ} and fraction of unstable modes f_{modes} from force constants of the same supercell ($\tau = 0.05\,\mathrm{eV\,\AA^{-2}}$, 20 000 wave vectors), with the deepest eigenvalue λ_{min} ($\mathrm{eV\,\AA^{-2}}$). The $6 \times 6 \times 6$ GRACE values used in Fig. 6 are 0.029 (Cu), 0.040 (Pd), 0.303 (W), 0.640 (Ti), 0.720 (Rh) and 0.327 (Al). Force constants are Fourier-interpolated with the minimum-image convention; without it the interpolation is exact only at commensurate wave vectors and biases f_{BZ} towards stability.

	Imaginary modes			f_{BZ}		f_{modes}		λ_{min}	
Phase	DFT	GRACE	DFT frequencies	DFT	GRACE	DFT	GRACE	DFT	GRACE
bcc Cu	12	12	30 (×12)	0.031	0.032	0.010	0.011	−0.24	−0.24
bcc Pd	12	12	24 (×12)	0.026	0.039	0.009	0.013	−0.28	−0.32
fcc W	16	16	35 (×16)	0.224	0.165	0.083	0.055	−1.34	−1.29
bcc Ti	20	20	38 (×8), 119 (×12)	0.607	0.600	0.258	0.204	−3.78	−2.42
bcc Rh	20	20	106 (×8), 127 (×12)	0.843	0.808	0.303	0.275	−7.66	−7.50
bcc Al	12	12	104 (×12)	0.310	0.322	0.103	0.107	−1.29	−1.27

The unstable zone fraction and the two regimes of SGTE

Supplementary Figure S4 contrasts two cases. In bcc Cu only one transverse branch is unstable, along Γ–N, the long-wavelength tail of $C' < 0$ confined to thin sheets of the zone; in bcc Ti the instability is deep at N (the Burgers mode towards hcp), near Γ and near P, and fills broad channels. f_{BZ} is 0.029 for Cu and 0.64 for Ti with $6\times6\times6$ force constants, and 0.030 and 0.59 with $4\times4\times4$; both are converged with the supercell. The SGTE lattice stability of bcc Cu equals its static energy (ratio 1.08); that of bcc Ti is 0.30 of it.

Figure 6 compares the extrapolated SGTE values with the static energy and with the depth along the softest-mode path (29 phases, panel a), and the entropy of the stable branches with measured and estimated entropies (panel b). Interpreting it requires knowing where the SGTE numbers come from (Methods): values for the transition, noble and simple metals were extrapolated from binary phase diagrams [13, 39, 40], those for the metallic structures of Si, Ge, As, Sb and Bi follow an estimate rule, and those for real high-temperature allotropes are fitted to experiment.

Within the extrapolated values (29 phases of 22 elements) two regimes appear (Fig. 6a). Lattices whose static energy exceeds the thermal energy at the melting point of the reference, $E_0 \gtrsim 0.8\,k_B T_m$, have SGTE values well below E_0 (19 of 20, ratio 0.13–0.75; the exception is bcc Al, whose value is the Kaufman–Bernstein estimate), and lattices with $E_0 < 0.8\,k_B T_m$ keep SGTE close to or above E_0 (7 of 9; the exceptions are hcp Pt, nearly stable on the potential, and bcc Co, treated non-magnetically here; Fisher's exact test $p = 2 \times 10^{-4}$). We read this as an empirical boundary in the present sample, not as a mechanism: E_0 is not a barrier along a particular path, and the melting point of the reference stands in for the upper temperature of the binary phase diagrams from which the values were extrapolated. The coefficient 0.8 was chosen after the fact as the best separation; values between 0.6 and 1.0 separate the sample almost equally well (Fisher's p between 1×10^{-3} and 2×10^{-4}), and a threshold on E_0 alone, between 12 and 15 kJ/mol, separates it as well as the scaled form. Extending the test to 24 further metallic phases that have an SGTE value but no descent path, all with $E_0 < 0.8\,k_B T_m$, confirms the weak regime in absolute terms (grey crosses in Fig. 6a; Supplementary Table S6): over the 33 phases below the boundary the SGTE value lies within 3 kJ/mol of E_0 in 24 cases and within 6 kJ/mol in 31, with a median $|a - E_0|$ of 1.4 kJ/mol (the two exceptions are hcp Fe, magnetic, and bcc Pd), and a follows E_0 with a slope of 0.91 ± 0.17, whereas above the boundary the median deviation is -18.6 kJ/mol, or $-0.63\,E_0$, and the slope is 0.31 ± 0.07. In the second regime the SGTE value is reproduced, without any fitted parameter, by the Born level along the softest-mode path: over the 26 extrapolated phases with a path, E_B reproduces SGTE with an RMS deviation of 4.9 kJ/mol, against 6.8 for the inflection-detection values of Chen et al. [24] (19 phases; 4.6 against 6.6 on the 17 phases common to both; bcc Co is left out of this comparison because Chen et al. refer it to fcc Co whereas SGTE and our levels refer to hcp Co) and 5.3 for the best single fraction, $0.38\,E_0$. The RMS advantage over inflection detection survives the removal of any single element (3.7–4.9 against 5.9–6.9 kJ/mol), but phase by phase the two are comparable: E_B is closer in 11 of 17 phases, and its smaller RMS comes from the absence of the large errors of inflection detection for Tc, Ir and Mo (per-phase table in Supplementary Table S5). E_B itself lies at 0.35–$0.69\,E_0$ for the strongly unstable lattices (a quartic Landau profile puts the inflection at $4E_0/9$), so the two observations are one: the level follows the depth of the double well along the path of the softest mode. f_{BZ} correlates with E_0 (Spearman's $\rho = 0.76$) and therefore with the ratio ($\rho = -0.48$, $p = 0.008$), but carries no information beyond E_0 (partial $\rho = -0.03$); bcc Al, Ni and Pt are unstable in 15–33 % of the zone, with imaginary modes of 104 cm^{-1} for Al in DFT, yet keep SGTE values at their static energies. The exceptions to the path rule are the bifurcating Bain paths of fcc Nb and V, where the softest mode gives $E_B = 0.05$ and

$0.15\,E_0$ and the SGTE value is matched instead by the level along the second unstable mode, the T_{2g} shear; we have no a priori rule that selects this route, so the softest-mode rule is stated with these two exceptions. Both statistics are exploratory, because the provenance classes were defined after the p-block values were seen to deviate, and because several phases share an element. The weakly unstable bcc Cu, Ag, Au and Pd and the strongly unstable bcc Rh, Ir, Tc and Os share the same source [40], so the split is not an artefact of who compiled which number; it agrees with the observation of Wang et al. that the discrepancy grows with the height of the energy maximum [14]. The p-block metallic structures do not follow the rule: fcc Si has $E_0 = 52\,\mathrm{kJ/mol}$ but an SGTE/static ratio of 0.98. Neither do the real allotropes. Both are consistent with their different provenance.

The temperature slopes b of the extrapolated values are not vibrational data (Methods). We therefore ask a narrower question: does the mean frequency of the stable part of the spectrum of the ideal unstable lattice track the entropy differences that the databases carry? Figure 6b compares the estimate ΔS_{harm} defined in the Methods with three references. For the phases of the noble and platinum metals and Mg assessed by Saunders et al. [40], ΔS_{harm} reproduces $-b$ within $1.0\,\mathrm{J\,mol^{-1}\,K^{-1}}$ RMS (the eight phases with $f_{\mathrm{used}} \geq 0.75$: the seven bcc phases of Mg, Au, Cu, Pd, Ag, Pt and Rh, all within 1.0, and hcp Pt, which deviates by 2.3): the melting-point convention encodes the softness of bcc relative to fcc. For the twelve real allotropes (f-block included) with $f_{\mathrm{used}} \geq 0.75$ and a measured transition it reproduces the magnitude of the transition entropies, 10 of 12 within $1.5\,\mathrm{J\,mol^{-1}\,K^{-1}}$, but not their ordering (Spearman's $\rho = -0.4$): on these twelve phases the RMS deviation of the estimate, $2.3\,\mathrm{J\,mol^{-1}\,K^{-1}}$, exceeds that of the constant mean of the reference values (0.7, or 0.8 with leave-one-out), so for the allotropes it reproduces the magnitude without predictive advantage over a constant, whereas for the Saunders phases it has one (1.0 against 1.3, or 1.5 with leave-one-out); it overestimates for bcc Th (8.6 against 2.2) and Sc (5.8 against 2.5); bcc La (5.5 against 3.3) falls just below the criterion ($f_{\mathrm{used}} = 0.735$) and is excluded, and hcp Ce, whose SGTE slope is zero by convention and which is therefore not a measured transition, deviates by 7.6. For the fcc and hcp phases of W and Mo it has the sign of the inflection-detection and molecular-dynamics values [18, 24] but is 1.5–2.5 times larger; against the 16 inflection-detection entropies of Chen et al. within the set it ranks correctly (Spearman's $\rho = 0.58$) with an offset of $+2.8\,\mathrm{J\,mol^{-1}\,K^{-1}}$. Within the set the deficit between the reference and the estimate does not correlate with f_{BZ}. This agrees with the statement that the vibrational entropy of a lattice ceases to be defined once the instability sets in [16]. In the present sample, for the 20 lattices of the set with a physical reference (the Saunders phases and the measured transitions), the estimate stays within $1.5\,\mathrm{J\,mol^{-1}\,K^{-1}}$ in 17 and within 3 in 18, with bcc Sc and Th as the exceptions, whereas for the fcc and hcp phases of W, Mo and Cr, whose SGTE slopes have the opposite sign to all later estimates, it deviates by 8–11; the correlation with measured and assessed entropies does not by itself make the estimate a thermodynamic quantity, and anharmonic contributions are not included.

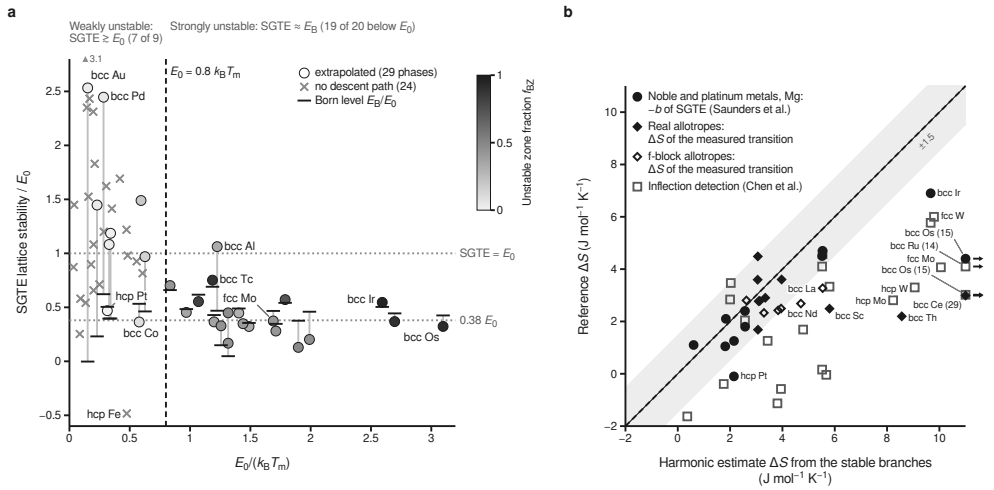

Fig. 6 What the extent of the instability does and does not control. (a) Ratio of the extrapolated SGTE lattice stability to the static energy against $E_0/(k_B T_m)$, the static energy over the thermal energy at the melting point of the reference phase, for the 29 extrapolated phases (circles; grey level: unstable zone fraction f_{BZ}, GRACE, $6 \times 6 \times 6$); bars: the Born level E_B along the softest-mode path (DFT scale) divided by E_0; dashed: the empirical boundary $E_0 = 0.8\, k_B T_m$; dotted: SGTE $= E_0$ and $0.38\, E_0$; crosses: 24 further metallic phases with an SGTE value but no descent path (mostly stable fcc and hcp phases; static energies from DFT or from the potential), one of them above the scale (triangle). Labels mark the phases discussed in the text; all values in Supplementary Table S6. (b) Harmonic estimate from the stable branches of the ideal unstable lattice (GRACE, $6 \times 6 \times 6$, 20 000 wave vectors) against the entropy of the measured transition for the real allotropes (SGTE fitted to experiment; filled diamonds, f-block open diamonds), the SGTE slope $-b$ for the phases of the noble and platinum metals and Mg assessed by Saunders et al. (circles), and the inflection-detection entropies of Chen et al. [24] (open squares). Grey band: $\pm 1.5\ \mathrm{J\,mol^{-1}\,K^{-1}}$ around the diagonal; labelled are the points outside it (of the inflection-detection values, only W and Mo); all values in Supplementary Table S7. bcc Ce, Os and Ru lie off scale (29, 15 and $14\ \mathrm{J\,mol^{-1}\,K^{-1}}$; arrows).

Discussion

Mechanical relaxation belongs to the family of mode-following methods [2, 3, 6, 8–10]. It differs from them in three respects. First, it follows the joint cell–atom Hessian instead of phonons at fixed cell, so strain and shuffle compete within one eigenproblem and every step is labelled by its strain fraction; the competition depends on the weight μ, which we state and vary. This is the bridge to TGLE, where only the strain part was used [29]. Second, it is applied to random symmetric starts in a blind set of space groups, not to a single high-symmetry parent, so the saddle network emerges from the statistics of trajectories. Third, it quantifies the cost of ordinary relaxation: three quarters of symmetric starts end on saddles. Saddle-point AIRSS [7] exploits the same fact in the opposite direction, imposing symmetry to collect saddles. Mechanical relaxation descends from them and keeps them as nodes of the map.

The extensive saddle order of the unstable lattices turns a long-standing qualitative statement, that unstable lattices have no harmonic free energy [16, 17], into a measurable quantity. In the sample and along the routes studied here, the thermodynamic coordinate is the path of the softest mode, the coordinate that TGLE follows:

its depth correlates with the lattice stability of a strongly unstable phase, and the mean frequency of the stable remainder of the spectrum reproduces the magnitude, though not the ordering, of the assessed entropies where that remainder makes up at least three quarters of the modes. f_{BZ}, by contrast, is a property of the lattice that DFT reproduces, but it is not a thermodynamic variable: the extrapolations assign to a lattice far above the ground state a fraction of its static energy, whether the lattice is unstable in a sliver or in a third of the zone. The level of an unstable phase is thus set by where the energy surface bends along the path to the stable one rather than by the volume of the unstable region. This is the inflection-point picture [17, 23, 24] seen from the path, as in self-consistent and anharmonic treatments [18–22], in which the depth of the instability, the shape of the surface and the temperature all enter. A direct test, left for future work, is to correlate the SGTE value with the inflection-point energy along the same mechanical-relaxation paths.

Mechanical relaxation ends at a point with no unstable mode of the joint Hessian *in the explored cell*; this is a local minimum with respect to the degrees of freedom of that cell, not a guarantee of stability at all wave vectors, and in 1.4 % of runs no push lowered the energy, so the run remains unresolved. It inherits the errors of the potential, such as lonsdaleite Si below diamond on GRACE, in contradiction with DFT. The saddle network is therefore potential-dependent. The supercell limits which wave vectors are accessible. Hcp→fcc requires three layers and double hcp four. Complex references such as β-U do not fit at all. The finite-difference Hessian costs $2(3N + 9)$ force evaluations per step, which is affordable with machine-learning potentials up to a few dozen atoms.

In summary, following the softest mode of the joint cell–atom Hessian until no unstable mode remains in the cell turns the saddles at which ordinary relaxation stops into a map whose hubs include the unstable lattices of CALPHAD. In this sample, the coordinate that TGLE follows is thus also the one on which the thermodynamic data appear to depend. Crystal structure prediction and the thermodynamics of unstable phases meet on the same object: the network of saddles.

Methods

Coordinates and the joint cell–atom Hessian

We work in the generalised coordinates of the Fréchet cell filter of ASE: the $3N$ Cartesian atomic coordinates (Å) and the nine components of the matrix logarithm of the deformation gradient, multiplied by a weight μ. With $\mu = N$, one unit of strain carries the weight of N atoms, which is the ASE default. The atomic coordinates are those of the undeformed cell, and the generalised force on the cell coordinates is the Fréchet derivative of the matrix exponential applied to the stress tensor times the volume [41], which at the reference cell reduces to the stress times the volume divided by μ; all Hessians below are finite differences of these generalised forces, so the mapping enters exactly. All derivatives, relaxations and descents of this paper are taken in these coordinates. The choice of μ is part of the method: it sets the relative scale of strain and displacement, and therefore can change which mode is softest and the strain fraction of a push. The saddle order of a stationary point does not depend

on it. We test the sensitivity to $\mu = N/4$ and $4N$ on 54 and 108 blind starts of Ti, Si, Sb and Bi (Supplementary Table S2). With $\mu = 4N$ the hits are nearly unchanged (32 against 34) and the first push stays a pure shuffle. With $\mu = N/4$ the first push becomes strain-dominated (median $c_w = 0.43$ against 0) and the hits drop from 14 to 8, mostly because Ti starts that reached hcp now end in fcc (7 cases): the strain-heavy push finds the packing but not the stacking (Results).

The joint Hessian is built by central differences of the generalised forces with a step of 0.005 in the generalised coordinates, that is $0.005\,\text{Å}$ for the atoms and $0.005/\mu = 0.005/N$ in strain for the cell, and is symmetrised. The three translations are projected out; the three rigid rotations of the cell remain as modes with $|\lambda| < 10^{-4}\,\text{eV}\,\text{Å}^{-2}$ and are never counted as unstable. The remaining eigenvalues λ_k and eigenvectors $\mathbf{u}_k$ describe all collective deformations of the cell and its contents. A mode is counted as unstable when $\lambda_k < -10^{-3}\,\text{eV}\,\text{Å}^{-2}$. Eigenvalues within 3 % of each other are grouped into degenerate subspaces. For each mode we record the strain fraction $c_w = \sum_{\text{cell}} u^2$, the squared norm of its nine cell components: $c_w = 1$ is a pure elastic-tensor mode, as in TGLE, and $c_w = 0$ is a pure shuffle.

For an $n \times n \times n$ supercell of a lattice with one atom per primitive cell, Bloch's theorem block-diagonalises the atomic part of the Hessian. Its eigenvectors are phonons at the n^3 commensurate wave vectors $\mathbf{q} = \mathbf{m}/n$, and its eigenvalues are the phonon branches $\lambda_b(\mathbf{q})$ in $\text{eV}\,\text{Å}^{-2}$, with $\omega^2 = \lambda/M$. The nine strain coordinates are the $\mathbf{q} \to 0$ acoustic limit. Mechanical relaxation in a finite cell therefore follows phonons on the grid of that cell together with the elastic modes.

Mechanical relaxation

Starting from the end point of ordinary relaxation, we diagonalise the joint Hessian. If unstable subspaces exist we take the softest one and choose a direction in it as follows. In a one-dimensional subspace the two candidates are $\pm\mathbf{u}$. In a two-dimensional subspace the candidates are $\cos\theta\,\mathbf{u}_1 + \sin\theta\,\mathbf{u}_2$ for $\theta = 0, 10^\circ, \ldots, 350^\circ$, refined to 0.5° around the best angle. In a subspace of dimension three or more they are 300 random unit vectors drawn once with a fixed seed, plus $\pm$ each basis vector. All candidates are scaled to the same Euclidean norm, and the one with the lowest energy at that norm is taken; ties are broken by the order of generation. This is Landau's criterion: at equal harmonic energy the anharmonic terms decide. The chosen direction is applied with three amplitudes $a = 0.02$, 0.08 and 0.2, scaled so that the largest atomic displacement equals a (Å) or the largest strain component equals a, whichever limit is reached first. Each trial is relaxed by fixed-step steepest descent in the same coordinates (step 0.01, halved whenever the energy rises, stopped when the generalised force falls below $0.004\,\text{eV}\,\text{Å}^{-1}$ or after 6000 steps), and the lowest end point is kept. The cycle is repeated until no unstable subspace remains, or for at most eight pushes; no run needed more than three pushes in the blind set or four in the targeted set. Nothing in the procedure is random beyond the fixed seed.

Starting structures, potential and DFT

Starting structures are random symmetric crystals generated by PyXtal [42] for a given space group and number of atoms N. The random state $1000\,g + 10N + i$ makes every start reproducible; rerunning six element–space-group pairs (36 starts) on different nodes reproduced every energy, space group and push bitwise. To avoid steering the search towards known answers, the *blind set* uses, for every element, the most frequent space group in the Inorganic Crystal Structure Database (ICSD) of each of the eleven Laue classes: $P\bar{1}$, $P2_1/c$, $Pnma$, $I4_1/a$, $I4/mmm$, $R\bar{3}$, $R\bar{3}m$, $P6_3/m$, $P6_3/mmc$, $Pa\bar{3}$ and $Fm\bar{3}m$. We use $N = 4$, 8, 12 and 16, with three starts each; the rhombohedral groups admit only $N = 12$. A *targeted set* that includes the space groups of the reference and of known polymorphs is reported in Supplementary Table S1. Structures are identified by their space group (spglib, tolerance 0.05 Å) and energy; a run "reaches the reference" when the end point has the space group of the SGTE reference structure and lies within 0.5 kJ/mol of it. Because a space group and an energy do not fix a structure, every hit was verified with spglib (tolerance 0.05 Å): the end structure must have the space group, the number of atoms in the primitive cell and the orbit sizes of the reference. 221 of 222 candidate hits pass; the exception, a Ga start that ends in a different $Cmce$ structure 0.4 kJ/mol above α-Ga, is counted as a miss for every scheme below, including ordinary relaxation. Nodes of the saddle network are structures with the same space group and energies within 0.5 kJ/mol; the saddle hubs were verified in the same way on the saddle frames of the trajectories: all 78 visits to the simple-cubic, bct and bcc hubs are the one-atom lattices, whereas of the seven saddle visits to the simple-hexagonal nodes of Si and Ge four are the one-atom lattice and three are a two-atom $P6/mmm$ structure, an AA-stacked honeycomb (Wyckoff position 2c) that the potential puts within 0.05 kJ/mol of the simple-hexagonal lattice and that spglib does not reduce at tolerances up to 0.3 Å (representative structures of every hub are described in the Supplementary Information, Section S9).

Ordinary relaxation is BFGS in the same coordinates (residual generalised force 0.005 eV Å^{-1}, at most 1500 steps). Energies and forces come from the foundation potential GRACE-2L-OMAT [30, 31]. Runs in which the potential collapses (end energy more than 100 kJ/mol below the reference, or a non-physical energy above 10^4 kJ/mol) are discarded: of 1254 generated blind starts, 33 (2.6 %) collapsed (Si 12, As 12, Ge 6, and one each of Bi, Ga and Sb), leaving 1221; of 648 targeted starts, 22 collapsed.

DFT checks use VASP with PAW-PBE potentials (Ti_sv, W_sv, Rh_pv, Ge_d, Bi_d; standard potentials otherwise), a 480 eV cutoff, Methfessel–Paxton smearing of 0.10 eV, fixed Γ-centred meshes with a spacing of 0.12 Å^{-1}, 10^{-8} eV electronic convergence, no spin polarisation and scalar-relativistic potentials. Hessians of $3 \times 3 \times 3$ and $4 \times 4 \times 4$ supercells are computed by finite differences (IBRION = 6, 0.015 Å) at fixed cell; the fixed-cell DFT Hessian is compared with the atomic block of the joint Hessian at the same cell. SGTE lattice stabilities are the intercepts a of linear fits $\Delta G = a + bT$ over 300–3000 K to the SGTE unary database [13]; static energies are DFT unless stated otherwise. For the test of f_{BZ}, the DFT eigenmodes of the $3 \times 3 \times 3$ cell are reconstructed into force constants and Fourier-interpolated exactly as for the potential.

Alternative schemes at accounted cost

We compare mechanical relaxation with three alternatives on the same blind starts, all beginning from the BFGS end point and all charged with every force evaluation, including those spent on Hessians: (i) following only the unstable modes of the fixed-cell atomic Hessian, followed by a full relaxation of atoms and cell, which is the scheme of Togo and Tanaka [8]; (ii) following only the unstable modes of the strain coordinates, which is the elastic step of TGLE; (iii) random pushes of the same amplitudes in the same coordinates, repeated while the energy decreases, with two realisations per start. One evaluation is one call of the potential returning energy, forces and stress; Hessians and the energies of the candidate scan are included, and because all schemes run on the same starts the distribution of cell sizes, and hence of the cost per call, is the same for all of them. The protocol matters: the atomic-mode scheme without the candidate scan and with six descents per push, as first implemented, solved 94 starts at twice the cost per hit (Supplementary Table S13).

Saddle order, fraction of unstable modes and unstable zone fraction

The *saddle order* n_- of an ideal lattice is the number of negative eigenvalues of its joint Hessian in $n \times n \times n$ supercells, $n = 1$–4. Two intensive quantities follow from the phonon branches. The *fraction of unstable modes*,

$$f_{\mathrm{modes}} = \lim_{N\to\infty} \frac{n_-}{3N} = \frac{1}{3} \left\langle \sum_{b=1}^{3} \mathbb{1}[\lambda_b(\mathbf{q}) < -\tau] \right\rangle_{\mathrm{BZ}}, \tag{1}$$

counts unstable branches, and the *unstable zone fraction*,

$$f_{\mathrm{BZ}} = \left\langle \mathbb{1}[\min_b \lambda_b(\mathbf{q}) < -\tau] \right\rangle_{\mathrm{BZ}}, \tag{2}$$

counts wave vectors at which at least one branch is unstable. They coincide only if all three branches are unstable wherever one is; when a single branch is unstable, $f_{\mathrm{modes}} = f_{\mathrm{BZ}}/3$. The six strain coordinates do not change either limit. We compute both from force constants of a $6 \times 6 \times 6$ supercell, Fourier-interpolated with the minimum-image (Wigner–Seitz) convention to 20 000 random wave vectors, with $\tau = 0.05\,\mathrm{eV\,Å^{-2}}$ to suppress interpolation noise; between $\tau = 0.001$ and $0.2\,\mathrm{eV\,Å^{-2}}$ the median f_{BZ} of the 61 metallic lattices moves from 0.35 to 0.31 and no classification below changes, and between $4 \times 4 \times 4$ and $6 \times 6 \times 6$ supercells the median change of f_{BZ} is 0.004 and the largest 0.07 (bcc Pt) (Supplementary Table S3). Unless stated otherwise, "unstable zone fraction" below means f_{BZ}. The minimum-image interpolation was verified on the EMT potential for bcc Cu: eigenvalues interpolated from $6 \times 6 \times 6$ force constants agree with exact $12 \times 12 \times 12$ values at commensurate wave vectors to $5 \times 10^{-6}\,\mathrm{eV\,Å^{-2}}$, $D(\mathbf{q})$ is Hermitian to 10^{-7} at random wave vectors, and f_{BZ} is 0.031 on both grids, whereas the same force constants without the convention give 0.003.

Born level along the softest-mode path

The Born level E_B is defined on the descent path from the ideal unstable lattice to its reference that follows the softest mode of the joint Hessian on the potential (one-atom cell for Bain-type paths, two-atom cell for the N-point shuffle, Euclidean-norm candidate scan). The frames of this descent are kept and their energies are recomputed with DFT. At each frame VASP (IBRION = 6, ISIF = 3, without symmetry reduction, ISYM = 0) displaces every atom by ± 0.015 Å along x, y and z and strains the cell by ± 0.5 % along the six Voigt components, $2(3N + 6)$ single-point calculations in all, and prints the forces and stresses of each perturbed configuration; from these the joint Hessian is assembled by least squares over the ± pairs in the same generalised coordinates as on the potential (atom–atom block from the forces under displacements, strain–strain block from the stresses under strains, mixed blocks from the forces under strains and the stresses under displacements, symmetrised, translations projected out). The matrix of perturbations has full rank $3N + 6$ in all 599 frames, and the asymmetry removed by the symmetrisation has a median of 0.03 eV Å^{-2} (maximum 0.6). After the same projection the atomic block of this Hessian agrees in sign with the phonon frequencies that VASP prints from its own force constants in 435 of the 443 frames with two or more atoms; the eight exceptions are modes between -0.05 and -0.005 eV Å^{-2}, below the 0.3 THz cutoff applied to the VASP frequencies. In one-atom cells the atomic block consists of the three translations only, and the imaginary frequencies of 0.30–0.35 THz that VASP prints for some of these frames are these translations, not instabilities (per-frame table in Supplementary Table S10). E_B is the DFT energy at which the smallest eigenvalue changes from negative to non-negative for the last time along the path, with the frames taken in the order of the descent and not sorted by energy (the DFT energy of the frames is not strictly monotonic on 5 of the 61 paths), interpolated linearly between the two bracketing frames; a level counts as confirmed only if every later frame of the path is stable. On 50 of the 61 paths the level is confirmed; on 9 the instability persists down to the lowest computed frame; bcc Yb shows only a change from stable to unstable within the window; and in bcc In the instability returns in the last two frames, so its level is not confirmed and the path is excluded from the statistics. The confirmed brackets have a median width of 0.76 kJ/mol (interquartile range 0.40–1.46, maximum 4.9 for bcc Re); this is the resolution of the discrete path, not an error bar, and the dependence of E_B on the route and on the cell, quantified next, is the larger uncertainty. VASP applies simple shears, which include a rotation, and correcting for it shifts E_B by at most 0.4 kJ/mol without changing its sign. On the potential, E_B differs between alternative routes that reach the reference by a median of 2.3 kJ/mol (interquartile range 0.7–6.7, maximum 21 for bcc Os) and is lower in the larger cell in 10 of the 11 paths with both cell sizes (median -2.0 kJ/mol). Frame-by-frame profiles for representative paths, the route and cell dependence for all paths and the full per-phase table are given in the Supplementary Information (Sections S6, S12 and S13).

Entropy estimate from the stable branches

The entropy estimate is a harmonic estimate from the stable branches: for each lattice we average $\ln\omega$ over the $(\mathbf{q}, b)$ pairs with $\lambda > \tau$ of the $6 \times 6 \times 6$ force constants and form $\Delta S_{\mathrm{harm}} = -3R\,(\langle \ln\omega\rangle_{\mathrm{lattice}} - \langle \ln\omega\rangle_{\mathrm{ref}})$, the classical high-temperature difference of two harmonic entropies with $3N$ modes each [16]. The unstable modes are not dropped from the sum: the estimate assigns to them the mean logarithmic frequency of the stable modes. It is therefore a descriptor of the stable part of the spectrum, not a partial harmonic entropy, and it is evaluated at the relaxed volume of each lattice without thermal expansion. The fraction of modes used, $f_{\mathrm{used}} = \frac{1}{3}\langle \sum_b \mathbb{1}[\lambda_b(\mathbf{q}) > \tau]\rangle_{\mathrm{BZ}}$, differs from $1 - f_{\mathrm{modes}}$ by the modes within $\pm\tau$ of zero, typically about 1 % of the modes (median 1.0 %, up to 6.8 % for bcc Ga in this set); it lies between 0.14 (bcc Ce) and 1.00. We adopt as applicability criterion that the estimate is reported only for lattices with $f_{\mathrm{used}} \geq 0.75$, which excludes bcc Ce, Hf, Ir, La, Nd, Os, Re, Ru and Tc, and we list the excluded values as well. Changing τ from 0.001 to 0.05 eV Å^{-2} changes ΔS_{harm} by 0.36 J mol^{-1} K^{-1} in the median and by at most 0.67 (bcc Sc; bcc Al 0.54), and from 0.05 to 0.2 eV Å^{-2} by 0.71 in the median and at most 1.63 (Sc), over the seven lattices of the set computed at all three thresholds, with the reference phase kept at $\tau = 0.05$, so that this is the sensitivity of the lattice term alone; the full table, including the excluded lattices, is in Supplementary Tables S7 and S12.

Provenance of the SGTE lattice stabilities

For the transition, noble and simple metals the SGTE values were obtained by extrapolating binary phase diagrams, combined with entropy-of-fusion rules. The sources are Kaufman and Bernstein [39], Saunders, Miodownik and Dinsdale [40] and later phase-diagram reassessments, all collected by Dinsdale [13]. For bcc Al the SGTE number is the Kaufman–Bernstein value, recently revisited [43]. For the metallic structures of Si, Ge, As, Sb and Bi the values follow an estimate rule that places them near the enthalpy of the liquid; for As and Sb the fcc, bcc and hcp enthalpies are identical. Real high-temperature allotropes (bcc Ti, Zr, Hf, Sc, Be, Yb, Y, Th) are fitted to experiment. The full provenance table is given in Supplementary Table S4. The intercept a is insensitive to the fitting range: over 52 phases the median change between 300–3000 K and 300–1500 K fits is 0.0 kJ/mol and the maximum 3.1 kJ/mol (real allotropes, whose $G(T)$ is non-linear), and no phase changes regime. The temperature slopes b of the extrapolated values are not vibrational data. They descend from entropies of fusion assigned by structure (2 and 2.15 cal mol^{-1} K^{-1} for bcc and fcc in Kaufman and Bernstein [39]), from an extrapolated metastable melting point combined with the correlation between the entropy and the temperature of fusion [40], or from group-wide constants (the fcc and hcp phases of V, Nb and Ta share one pair of slopes); for fcc and hcp W and Mo their sign is opposite to every later estimate [18, 24].

Use of AI tools

AI assistants (Claude, Anthropic) were used for code development, language editing, the layout of figures from the computed data and automated consistency checks of the

numbers in the text against the data. All calculations were run and all results were checked by the authors, who take full responsibility for the content.

Data availability. All data generated or analysed during this study are included in this published article and its supplementary information files. The raw VASP output files (OUTCAR) are available from the corresponding author on reasonable request.

Code availability. The implementation of mechanical relaxation and the scripts that regenerate every number and figure are included in the supplementary information files of this article.

Acknowledgements. The authors express their sincere gratitude and respect to the Armed Forces of Ukraine, who made it possible to complete the preparation of this article for publication. The authors thank Al-Bayan University, Baghdad, Iraq, for its great support of scientific research. This research utilised Queen Mary's Apocrita HPC facility, supported by QMUL Research-IT, http://doi.org/10.5281/zenodo.438045.

Funding. This research was funded by the Ministry of Education and Science of Ukraine, grant number 0124U000668. The collaboration was further supported by the Royal Society International Exchanges Scheme (Grant No. IES\R2\232244).

Author contributions. P.P. conceived the study, developed the method and the software, performed the calculations and the analysis, prepared the figures and wrote the manuscript. T.A.S., A.Z. and G.A.C. contributed to the discussion and interpretation of the results and revised the manuscript critically. All authors reviewed the manuscript.

Competing interests. The authors declare no competing interests.

Additional information. Supplementary Information accompanies this paper. Correspondence and requests for materials should be addressed to P.P.

References

[1] Pickard, C. J. & Needs, R. J. Ab initio random structure searching. *J. Phys.: Condens. Matter* **23**, 053201 (2011).

[2] Lyakhov, A. O., Oganov, A. R. & Valle, M. How to predict very large and complex crystal structures. *Comput. Phys. Commun.* **181**, 1623–1632 (2010).

[3] Lyakhov, A. O., Oganov, A. R., Stokes, H. T. & Zhu, Q. New developments in evolutionary structure prediction algorithm USPEX. *Comput. Phys. Commun.* **184**, 1172–1182 (2013).

[4] Lenz, M.-O. *et al.* Parametrically constrained geometry relaxations for high-throughput materials science. *npj Comput. Mater.* **5**, 123 (2019).

[5] Pallikara, I., Kayastha, P., Skelton, J. M. & Whalley, L. D. The physical significance of imaginary phonon modes in crystals. *Electron. Struct.* **4**, 033002 (2022).

[6] Conway, L. J., Pickard, C. J. & Hermann, A. in *First principles crystal structure prediction* (eds Reedijk, J. & Poeppelmeier, K. R.) *Comprehensive Inorganic Chemistry III*, Vol. 3 393–420 (Elsevier, 2023).

[7] Monserrat, B. *et al.* Structure and metallicity of phase V of hydrogen. *Phys. Rev. Lett.* **120**, 255701 (2018).

[8] Togo, A. & Tanaka, I. Evolution of crystal structures in metallic elements. *Phys. Rev. B* **87**, 184104 (2013).

[9] Naruse, T., Seko, A. & Tanaka, I. Global structure optimization following imaginary phonon modes accelerated by machine learning potentials in Cu, Ag, and Au. *J. Ceram. Soc. Jpn.* **131**, 746–750 (2023).

[10] Naruse, T., Seko, A. & Tanaka, I. A systematic approach to crystal structure prediction following imaginary phonon modes combined with polynomial machine learning potentials. *J. Phys. Soc. Jpn.* **94**, 074601 (2025).

[11] Stokes, H. T. & Hatch, D. M. Procedure for obtaining microscopic mechanisms of reconstructive phase transitions in crystalline solids. *Phys. Rev. B* **65**, 144114 (2002).

[12] Trinkle, D. R., Hatch, D. M., Stokes, H. T., Hennig, R. G. & Albers, R. C. Systematic pathway generation and sorting in martensitic transformations: Titanium α to ω. *Phys. Rev. B* **72**, 014105 (2005).

[13] Dinsdale, A. T. SGTE data for pure elements. *Calphad* **15**, 317–425 (1991).

[14] Wang, Y. *et al.* Ab initio lattice stability in comparison with CALPHAD lattice stability. *Calphad* **28**, 79–90 (2004).

[15] Skriver, H. L. Crystal structure from one-electron theory. *Phys. Rev. B* **31**, 1909–1923 (1985).

[16] Grimvall, G., Magyari-Köpe, B., Ozoliņš, V. & Persson, K. A. Lattice instabilities in metallic elements. *Rev. Mod. Phys.* **84**, 945–986 (2012).

[17] van de Walle, A., Hong, Q., Kadkhodaei, S. & Sun, R. The free energy of mechanically unstable phases. *Nat. Commun.* **6**, 7559 (2015).

[18] Ozoliņš, V. First-principles calculations of free energies of unstable phases: the case of fcc W. *Phys. Rev. Lett.* **102**, 065702 (2009).

[19] Souvatzis, P., Eriksson, O., Katsnelson, M. I. & Rudin, S. P. Entropy driven stabilization of energetically unstable crystal structures explained from first principles theory. *Phys. Rev. Lett.* **100**, 095901 (2008).

[20] Hellman, O., Abrikosov, I. A. & Simak, S. I. Lattice dynamics of anharmonic solids from first principles. *Phys. Rev. B* **84**, 180301 (2011).

[21] Asker, C., Belonoshko, A. B., Mikhaylushkin, A. S. & Abrikosov, I. A. First-principles solution to the problem of Mo lattice stability. *Phys. Rev. B* **77**, 220102 (2008).

[22] Kadkhodaei, S., Hong, Q.-J. & van de Walle, A. Free energy calculation of mechanically unstable but dynamically stabilized bcc titanium. *Phys. Rev. B* **95**, 064101 (2017).

[23] van de Walle, A. Invited paper: Reconciling SGTE and ab initio enthalpies of the elements. *Calphad* **60**, 1–6 (2018).

[24] Chen, H., Hong, Q.-J., Navrotsky, A. & van de Walle, A. A computational free energy reference for mechanically unstable phases. *Calphad* **91**, 102869 (2025).

[25] Sluiter, M. H. F. Ab initio lattice stabilities of some elemental complex structures. *Calphad* **30**, 357–366 (2006).

[26] Turchi, P. E. A. *et al.* Interface between quantum-mechanical-based approaches, experiments, and CALPHAD methodology. *Calphad* **31**, 4–27 (2007).

[27] Wales, D. J. *Energy Landscapes: Applications to Clusters, Biomolecules and Glasses* (Cambridge University Press, 2003).

[28] Wales, D. J. Exploring energy landscapes. *Annu. Rev. Phys. Chem.* **69**, 401–425 (2018).

[29] Prysyazhnyuk, P., Di Tommaso, D. & Ivanov, O. Tensor-guided lattice exploration (TGLE): Directed crystal structure search based on elastic eigenmodes. *ChemRxiv* (2026). Preprint at https://doi.org/10.26434/chemrxiv.15004734/v1.

[30] Bochkarev, A., Lysogorskiy, Y. & Drautz, R. Graph atomic cluster expansion for semilocal interactions beyond equivariant message passing. *Phys. Rev. X* **14**, 021036 (2024).

[31] Lysogorskiy, Y., Bochkarev, A. & Drautz, R. Graph atomic cluster expansion for foundational machine learning interatomic potentials. *npj Comput. Mater.* **12**, 114 (2026).

[32] Needs, R. J., Martin, R. M. & Nielsen, O. H. Total-energy calculations of the structural properties of the group-V element arsenic. *Phys. Rev. B* **33**, 3778–3784 (1986).

[33] Silas, P., Yates, J. R. & Haynes, P. D. Density-functional investigation of the rhombohedral to simple-cubic phase transition of arsenic. *Phys. Rev. B* **78**, 174101 (2008).

[34] Gaspard, J.-P. Structure of covalently bonded materials: From the Peierls distortion to phase-change materials. *C. R. Physique* **17**, 389–405 (2016).

[35] Shell, M. S., Debenedetti, P. G. & Panagiotopoulos, A. Z. Saddles in the energy landscape: extensivity and thermodynamic formalism. *Phys. Rev. Lett.* **92**, 035506 (2004).

[36] Broderix, K., Bhattacharya, K. K., Cavagna, A., Zippelius, A. & Giardina, I. Energy landscape of a Lennard-Jones liquid: statistics of stationary points. *Phys. Rev. Lett.* **85**, 5360 (2000).

[37] Angelani, L., Di Leonardo, R., Ruocco, G., Scala, A. & Sciortino, F. Saddles in the energy landscape probed by supercooled liquids. *Phys. Rev. Lett.* **85**, 5356 (2000).

[38] Doye, J. P. K. & Wales, D. J. Saddle points and dynamics of Lennard-Jones clusters, solids, and supercooled liquids. *J. Chem. Phys.* **116**, 3777 (2002).

[39] Kaufman, L. & Bernstein, H. *Computer Calculation of Phase Diagrams* (Academic Press, 1970).

[40] Saunders, N., Miodownik, A. P. & Dinsdale, A. T. Metastable lattice stabilities for the elements. *Calphad* **12**, 351–374 (1988).

[41] Larsen, A. H. *et al.* The atomic simulation environment—a Python library for working with atoms. *J. Phys.: Condens. Matter* **29**, 273002 (2017).

[42] Fredericks, S., Parrish, K., Sayre, D. & Zhu, Q. PyXtal: A Python library for crystal structure generation and symmetry analysis. *Comput. Phys. Commun.* **261**, 107810 (2021).

[43] van de Walle, A. *et al.* Revisiting the SGTE lattice stability of bcc aluminum. *Calphad* **83**, 102628 (2023).

Supplementary Files

This is a list of supplementary files associated with this preprint. Click to download.

- 03SupplementaryInformation.pdf
- 06datapackage20261105scireprev1.zip